nature materials

SUPPLEMENTARY INFORMATION

DOI: 10.1038/NMAT3826

Crossover from incoherent to coherent phonon scattering in epitaxial oxide superlattices

Jayakanth Ravichandran,[1,2]‡† Ajay K. Yadav,[2,3]† Ramez Cheaito,[4]† Pim B. Rossen,[3] Arsen Soukiassian,[5] S. J. Suresha,[2] John C. Duda,[4] Brian M. Foley,[4] Che-Hui Lee,[5] Ye Zhu,[6] Arthur W. Lichtenberger,[7] Joel E. Moore,[2,8] David A. Muller,[6,9] Darrell G. Schlom,[5,9] Patrick E. Hopkins,[4] Arun Majumdar,[10] R. Ramesh,[1,2,3,8,11*] and Mark A. Zurbuchen[12,13,14*]

Affiliations:

[1]Applied Science and Technology Graduate Group, University of California, Berkeley, CA 94720, USA.

[2]Materials Sciences Division, Lawrence Berkeley National Laboratory, Berkeley, CA 94720, USA.

[3]Department of Materials Science and Engineering, University of California, Berkeley, CA 94720, USA.

[4]Department of Mechanical and Aerospace Engineering, University of Virginia, Charlottesville, VA 22904, USA.

[5]Department of Materials Science and Engineering, Cornell University, Ithaca, NY 14853, USA.

[6]School of Applied and Engineering Physics, Cornell University, Ithaca, NY 14853, USA.

[7]Department of Electrical and Computer Engineering, University of Virginia, Charlottesville, VA 22904, USA.

[8]Department of Physics, University of California, Berkeley, CA 94720, USA.

[9]Kavli Institute at Cornell for Nanoscale Science, Cornell University, Ithaca, NY 14853, USA.

[10]ARPA-E, US Department of Energy, 1000 Independence Avenue, Washington, DC 20585, USA.

[11]Oak Ridge National Laboratory, Oak Ridge, TN 37831, USA.

[12]Department of Materials Science and Engineering, University of California, Los Angeles, CA 90095, USA.

[13]Western Institute of Nanoelectronics, Department of Electrical Engineering, University of California, Los Angeles, CA 90095, USA

[14]California NanoSystems Institute, University of California, Los Angeles, CA 90095, USA.

‡Present address: Department of Physics, Columbia University, New York, NY 10027, USA.

†These authors contributed equally to this work.

*To whom correspondence should be addressed. E-mail: rramesh@berkeley.edu or mark_z@mac.com

DOI: 10.1038/NMAT3826

MATERIALS AND METHODS

A) Synthesis of superlattices:

1) Laser MBE:

Superlattices of $(STO)_m/CTO)_n$ were synthesized using reflection high energy electron diffraction (RHEED) assisted laser MBE (l-MBE). These $(STO)_m/(CTO)_n$ superlattices were grown on $(001)_{pc}$-oriented single-crystal $NdGaO_3$ (NGO), $(LaAlO_3)_{0.3}$-$(Sr_2AlTaO_6)_{0.7}$ (LSAT) and $SrTiO_3$ (STO) substrates to further study the effect of a small in-plane strain of -0.1%, -0.15%, and 0.93%, respectively. The targets used for the growth were single crystalline STO and sintered, polycrystalline CTO. The growth temperature was set at 700°C to ensure stoichiometric transfer of both CTO and STO. The growth pressure employed was 50 mTorr with a laser fluence of 1.5 Jcm^{-2}. The growth was monitored using RHEED with Frank-van der Merwe layer-by-layer growth mode present throughout the growth process (details are provided in the supplementary section). The specular spot exhibited well-defined oscillations with changes in the coverage of the substrate, and this enabled controlled growth of the superlattices with different period-thicknesses while achieving the same total thickness. In Figure S1a we show variation of the intensity of the specular spot for the first 10 periods of an $(STO)_2/(CTO)_2$ superlattice. The RHEED oscillations were monitored for the specular spot along the [1 $\bar{1}$ 0] direction of the $NdGaO_3$ $(100)_{pc}$ substrate. Figure S1b shows the RHEED pattern for the substrate before growth and the superlattice after growth. The specular spot and the diffraction spots are still clearly visible, also corroborating our claim of excellent smoothness of the surface after a 200 nm film growth. After the growth, the samples were cooled to room temperature in 50 Torr of oxygen partial pressure to ensure oxygen stoichiometry of the samples.

2) Oxide MBE:

$(STO)_m/(BTO)_n$ and $(STO)_m/CTO)_n$ superlattices were synthesized by reactive MBE[1-7] in Veeco 930 and Gen 10 MBE systems. This physical vapour deposition technique enables the growth of superlattice with atomic layer precision through the use of *in situ* monitoring of RHEED oscillations. Superlattices were fabricated by supplying the substrate with precise single monolayer doses of CaO, SrO, BaO and TiO_2 in the layer order of the desired superlattice at a substrate temperature of ~650 °C in a background pressure of 5×10^{-7} Torr of molecular oxygen. Four-circle x-ray diffraction measurements confirmed that all of the superlattices on which thermal conductivity measurements were made were commensurate with the underlying substrates. A detailed account of the growth and structural characterization of $(STO)_m/(BTO)_n$ superlattices can be found elsewhere[3]. Film quality for both growth techniques was characterized by x-ray diffraction (XRD), atomic force microscopy (AFM) and transmission electron microscopy (TEM), which are discussed in detail in section D.

B) Thermal Conductivity Measurements

We measure the thermal conductivity of our samples with time domain thermoreflectance (TDTR)[8,9]. TDTR is a pump-probe technique in which the laser output of a mode-locked Ti:Sapphire oscillator is split into two paths: a pump path that creates a modulated heating event on the sample surface and a time-delayed probe path that monitors the temperature of the pump heating event as a function of time. A schematic of the main components in the experiment used at the University of Virginia is shown in Figure S2 and described henceforth. The experiment is centred on a short pulsed oscillator that operates at 80 MHz repetition rate with pulses centred at 800 nm and pulse widths of ~300 fs at the sample surface. The pump path is modulated with an

DOI: 10.1038/NMAT3826

electro-optic modulator driven by a sinusoidal modulation waveform at a frequency of 11.4 MHz. The pump then undergoes a second harmonic generation in a BIBO crystal that converts the 800 nm light to 400 nm. This simplifies alignment and increases signal to noise ratio by easily blocking any scattered pump light through efficient colour filters at the detection optics. A mechanical delay stage is used to delay the arrival of the probe to the sample surface. The stage gives time delays up to 5 ns. The pump and probe beams are then coaxially focused by a microscope objective to roughly 24.5 μm and 10 μm radii at the sample surface, respectively, eliminating any sensitivity to in-plane heat transfer. The microscope objective can be used to view the image of the sample on a CCD camera. The reflected probe is directed to a photo-detector connected to the RF lock-in amplifier. Because of the periodic heating created by pump modulation on the sample surface, the reflected probe contains a frequency component at the pump modulation. The same modulation frequency is supplied to the lock-in amplifier as a reference frequency. We use the ratio of the in-phase and out-of-phase components of the thermoreflectance signal detected by the lock-in amplifier to monitor the surface temperature decay over the full time delay range. All the studied samples were coated with a thin Aluminum film that acts as temperature transducer. We measure the thickness of the Al films during each measurement with picosecond ultrasonics[10,11]. We perform 4-5 measurements on each sample at different locations. We assume literature values for the heat capacity and thermal conductivity of the Al film[12]. We treat the SL film as one layer of weighted average of the bulk heat capacity values of CTO[13] and STO[14] for the $(STO)_m/(CTO)_n$ superlattices and for the STO and BTO for the $(STO)_m/(BTO)_n$ superlattices. The thermal conductivity of the NGO substrate is measured separately using a reference NGO sample from the same lot as the substrate on which the samples were grown. Hence the only unknowns in our thermal model are the Al/superlattice

Kapitza conductance, h_1, the thermal conductivity of the SL film, κ, and Kapitza conductance between the SL and the substrate, h_2.

The thermal penetration depth into the sample, defined as the depth from the surface at which the temperature drops to e^{-1} of its surface value[15], can be estimated by (eqn. (1)):

$$\delta(T) = \sqrt{\kappa(T)/(\pi C(T) f)} \quad (1)$$

where, κ and C are the thermal conductivity and volumetric heat capacity of the substrate, respectively, f is the pump modulation frequency and T is the temperature. Substituting 11.4 MHz for the modulation frequency and reasonable values for heat capacity and thermal conductivity, the thermal penetration depth is estimated to be between ~200 and 630 nm for temperatures in the range 80 - 300 K. As a result we expect that h_2 will have a great effect at low temperatures. For this reason we revert to studying the sensitivity of the measurement to this parameter and the other parameters of interest.

The sensitivity of the ratio[16] used in the analysis (eqn. (2)) is defined by:

$$S_x = \frac{\partial ln(\frac{-V_{in}}{V_{out}})}{\partial lnx} \quad (2)$$

where x is the parameter of interest, V_{in} is the lock-in in-phase component, and V_{out} is the lock-in out-of-phase component. Figure S3 shows the sensitivity of the ratio to h_1, κ, and h_2 for the temperatures 84 K, 142 K and 306.7 K. These figures were plotted for typical experimental conditions and assuming reasonable values for the layers' thermal conductivities and heat capacities, and the interface conductances between layers. The figure shows that at 84 K, the sensitivity to h_2 is significant whereas at 142 K the sensitivity to h_1 and h_2 becomes negligible compared to the sensitivity to κ. As a result, and only at 84 K and 110 K, we perform the measurement at two other frequencies, 1.5 MHz and 3.5 MHz in addition to the 11.4 MHz. Performing the measurement at 3 different frequencies allows us to estimate the value of h_2. We

DOI: 10.1038/NMAT3826

manually adjust h_2 so that the best fits of the three different measurements yield the same values for h_1 and κ where h_1 and κ are treated as free parameters and are varied to fit the data to a multilayer thermal model[9,17,18]. We find that at 84 K, $h_2 \sim 30 - 40\ MWm^{-2}K^{-1}$ and at 110 K, $h_2 \sim 40 - 50\ MWm^{-2}K^{-1}$. Values higher than $60\ MWm^{-2}K^{-1}$ at higher temperatures will make the sensitivity to h_2 negligible compared to κ.

Figure S4 shows a sample data and best-fit curves for a $(STO)_1/(CTO)_1$ and a $(STO)_3/(CTO)_3$ superlattice samples on NGO (110) substrate at 306.7 K.

We account for the steady state temperature rise in the sample due to the laser power absorbed by the sample (eqn. (3))[17] using

$$\Delta T = \frac{(A\dot{Q})_0 + (A\dot{Q})_1}{\kappa(2\pi w_0^2 + 2\pi w_1^2)^{1/2}} \quad (3)$$

where A is the absorption of Aluminum, $\dot{Q}$ is the power of the pump or probe, the subscripts "0" and "1" refer to the pump and probe, respectively, κ is the thermal conductivity of the heat sink which is NGO in this case, w_0 and w_1 are the pump and probe radii, respectively. For our experimental conditions we put 30 mW of total power into the sample at low temperatures and 45 mW at room temperature. This gives ~ 3-10 K temperature rise for temperatures between 80 and 296 K. At low temperatures, even a very minor error in the temperature can lead to an appreciable error in the literature values assumed for the heat capacities of Aluminum, the film and substrate causing a significant error in the best fit values in thermal conductivity. The error bars in our data shown in Figures 1 and 2 of the manuscript account for the standard deviation in the measurement and the uncertainty in the Al transducer thickness.

Figure S5 shows the measured thermal conductivity of 200-nm STO and CTO films as a function of temperature. Both the samples show a maximum in thermal conductivity indicating that the Umklapp phonon scattering becomes the dominant phonon scattering mechanism. The

thermal conductivity values of the STO films are slightly lower than the values reported elsewhere, due to the presence of small amount point defect impurities[19]. The growth temperature was chosen to ensure that both the materials of the superlattice could grow with the highest possible structural integrity.

Figure S6 shows the thermal conductivity values of STO/BTO superlattices measured at 80 and 300 K respectively. Even though the minimum is observable at 80 K, it is not extremely pronounced. The reason for this is discussed in the theoretical calculations part.

C) Theoretical Calculations

1) Modified Simkin-Mahan model (SM Model)

We used a simple model devised by Simkin and Mahan[20] (SM Model) with two minor modifications to improve its relevance to our experiments. The first modification is to model differences in volume fraction of the species and the second modification is to model potential interface disorder in the studied films. The latter is necessary because the original model, while it includes a bulk mean free path, does not include the effect of additional disorder at interfaces. As described below, only a small disorder-induced thermal boundary resistance is required to explain the data. The interface density dependence of the thermal conductance in the theoretical model was determined by the following parameters: the mass ratio of the two materials, one mean free path for the bulk materials, an interface thermal conductance, and (for one system) the volume fraction of the material. We separately discuss incorporation of an interface-density-dependent mean free path, which gives comparable results and a microscopic picture of the effects of increased disorder at interfaces.

DOI: 10.1038/NMAT3826

The approach of the SM model, which we retain, is to compute the phonon band structure for a perfect lattice with a super-cell containing one period of the superlattice, then add an imaginary part *i/l* to the wave vector, where *l* is the mean free path parameter. The thermal conductance is then obtained via the standard thermal sum over phonon modes. The original model does not incorporate any additional disorder due to the interfaces and retains the same lattice spacing for the materials making up the superlattice.

Currently the model does not account for the effect of octahedral distortions/tilting of $SrTiO_3$ in the superlattices, and this aspect is the focus of on-going efforts. The calculated thermal conductivity of $(STO)_m/(CTO)_n$ superlattices as a function of interface density is shown for different mean free path (λ) values in Figure S7. The atomic mass ratio and group velocities were the only input parameters required to perform these calculations and the model employed a 50:50 volume fraction ratio. The calculated thermal conductivity using the SM Model was rescaled to actual thermal conductivities by multiplying by a constant factor determined by the low interface density limit. In the case of $(STO)_m/(CTO)_n$ superlattices, the thicknesses and volume fraction were kept constant, so the only fitting parameter employed was the interface disorder. The interface disorder component was modelled as a thermal resistance (eqn. (4)), which scales linearly with the interface density given as:

$$\frac{1}{k_{expt}} = \frac{1}{k_{SM}} + \frac{n}{G} \qquad (4)$$

where, n is the interface density, G is disorder thermal conductance, k_{expt} and k_{SM} are the experimentally measured thermal conductivities and rescaled thermal conductivity calculated from the SM model. The interface disorder thermal conductance values used for the model calculations shown in Figure 1a,b were 48 $GWm^{-2}K^{-1}$ and 18 $GWm^{-2}K^{-1}$, respectively. These thermal conductance values in terms of equivalent oxide thickness are 0.21 and 0.56 Å,

respectively and these values are one order of higher than the highest thermal interface conductances ever reported[21]. This suggests that the presence of even a very small disorder is clearly detrimental to the observation of the thermal conductivity minimum.

In the case of the $(STO)_m/(BTO)_n$ superlattices, we employed two other corrections such as the volume fraction and size effects, in order to account for the differences between the employed model and experimental samples. The effect of volume fraction variation was accounted for with a correction factor, which considered the bulk thermal conductivities in a series resistance model (eqn. (5)) as given below.

$$f = \frac{\frac{200\,k_A k_B}{k_A + k_B}}{\left[\left(\frac{x}{k_A}\right) + \left(\frac{100-x}{k_B}\right)\right]} \tag{5}$$

where, k_A *and* k_B are bulk thermal conductivities of the two component and x is the volume fraction of component A. It is worth noting that in all these analyses so far, we have ignored the corrections due to the size effects. The role of size effects on measured thermal conductivity values of alloys is discussed in detail elsewhere[22]. It is worth noting that such an effect becomes more important at lower temperatures and hence any analysis of superlattice thermal conductivity to uncover wave effects will have to account for variations in thickness and the other corrections discussed above. This is precisely the reason why the minimum in the thermal conductivity of $(STO)_m/(BTO)_n$ superlattices at low temperature is not more pronounced.

An approach to incorporating interface disorder within the Simkin-Mahan model is as follows. It is assumed that extra scattering at the interface leads to an additional contribution to the mean free path that adds via Mathiessen's rule to the bulk mean free path parameter:

$$\frac{1}{\lambda(L)} = \frac{c}{L} + \frac{1}{l}.$$

DOI: 10.1038/NMAT3826

Here c is a constant that determines the effectiveness of additional interface scattering. We have evaluated the relative thermal conductivity of STO/CTO superlattices for the interface density dependent m.f.p model as shown in Figure S8, for values c = 0.0 (the unmodified model), 0.01, 0.02, 0.03 and a bulk mean free path l=30. The main effect of these small values of c is to suppress the maximum at (1,1), just as was the effect of the small thermal boundary resistance. We conclude from the similarity in the results of these two approaches that our data are consistent with either modification of the Simkin-Mahan model to include additional interface scattering.

2) Coherence length calculations

The wave-particle crossover occurs at the mean free path parameter in the theoretical model of the above calculations (SM model, Sec. C1). To describe the wave processes such as ballistic or coherent phonon transport, we should estimate this mean free path parameter from the phonon coherence length.[23] Hence, we use the coherence length as a qualitative estimate for the suitability of a materials system for demonstrating such a wave-particle crossover. The phonon coherence length calculations were performed using a method reported elsewhere[23]. An averaged Debye-like dispersion was assumed for all the acoustic branches; the contributions of the optical branches were ignored. It is important to realize that these are qualitative estimations and one must consider the full dispersion for fully accurate coherence-length calculations. Realistic zone edge cut-off frequencies and group velocities for GaAs[24] and $SrTiO_3$[12,25] were obtained from appropriate references. The calculations showed very weak temperature dependence over a temperature range of 100-300 K. This trend is consistent with the results reported for GaAs[23].

D) Structural characterization

1) X-ray Diffraction

All the films were characterized by x-ray diffraction with a Panalytical X'Pert Pro diffractometer using Cu-K_α radiation. We have collected extensive reciprocal-space maps of the superlattice samples to rule out the possibility of strain relaxation, and hence inferring the absence of misfit dislocations. Particularly, it is necessary to show that the samples with interface density around the thermal conductivity minimum are of high crystalline quality and do not have any other defects such as other dislocations causing the observed non-monotonic thermal conductivity trend. The reciprocal space maps for different samples with varying periodicity such as (a) $(STO)_1/(CTO)_1$ (b) $(STO)_3/(CTO)_3$ (c) $(STO)_6/(CTO)_6$ and (d) $(STO)_9/(CTO)_9$ are shown in Figure S9. It is evident that the superlattices remain coherently strained to the substrate for all these periods, which span the entire thermal conductivity minimum.

Long-range θ-2θ XRD scans of the $(STO)_m/(BTO)_n$ samples used for the temperature-dependent TDTR study in Figure S6 are shown in Figure S10 a,b, in order of increasing interface density from the bottom up. Panel A corresponds to the four samples with high interface densities. Panel B corresponds to the two lowest interface density samples. It is evident from the many orders of peaks arising from the superlattices that these samples have exceptional long-range order, with sharp interfaces. Figure S10 b shows a representative rocking curve for the $(STO)_4/(BTO)_3$ sample, with the superlattice exhibiting a degree of crystalline perfection commensurate with that of the underlying substrate, indicating a very low degree of crystal mosaic, and thus a low density of dislocations that could affect its thermal conductivity. These data validate our TDTR results.

DOI: 10.1038/NMAT3826

2) Atomic Force Microscopy

Surface topography of superlattice films were recorded using a Digital Instruments Nanoscope-IV Multimode AFM, under ambient conditions. Figure 3d of the manuscript is a 2.5 μm by 5 μm tapping-mode AFM image (obtained in air) of flattened $(STO)_2/(CTO)_2$, an illustration of surface topography in these perovskite superlattices. Figure S11 also provides a cross-sectional profile along the line X—X', revealing steps of height 3.8 Å, which is approximately equal to the unit cell of CTO. The presence of atomic steps shows that 200-nm thick superlattice films are atomically smooth, with RMS roughness of 3.0 Å. In addition, the atomic steps, combined with RHEED oscillations, further confirm the growth mechanism of these superlattice films to be Frank-Van der Merwe (layer-by-layer).

3) Transmission Electron Microscopy (TEM)

Samples for scanning transmission electron microscopy (STEM) observations reported on $(STO)_m/(BTO)_n$ superlattices were prepared in cross-section by mechanical wedge polishing, followed by limited time Ar-ion milling[26]. High-angle annular-dark-field (HAADF) STEM images were taken on a 200 kV FEI Tecnai F20 SuperTWIN STEM. Electron energy loss spectroscopy (EELS) maps for Ti and Ba elements were acquired on a 100 kV NionUltraSTEM, using Ti-$L_{2,3}$ edges and Ba-$M_{4,5}$ edges, respectively. Additional TEM characterization was carried out on samples prepared in FEI FIBs, and were subsequently examined in bright field, high-resolution TEM (HRTEM), and HAADF-STEM modes at 300 keV. Figure S12a,b show HAADF-STEM images of the $(STO)_{30}/(BTO)_1$ sample at low and high magnification in a and b, respectively, providing further verification of the significant long-range order and the presence of unit-cell-sharp interfaces.

Electron-transparent cross-sectioned samples of $(STO)_m/(CTO)_n$ superlattices were prepared by wedge polishing followed by low-energy low-angle argon ion milling on a liquid-nitrogen-cooled stage. HAADF-STEM on $(STO)_m/(CTO)_n$ superlattice samples was carried out using the TEAM 0.5 microscope (a modified FEI Titan 80-300 equipped with a CEOS aberration corrector) operated at 300 kV, located at the National Center for Electron Microscopy (NCEM) at the Lawrence Berkeley National Laboratory. A probe semi-convergence angle of 17.2 mrad was used. The HAADF detector was set to collect electrons scattered between 70 and 290 mrad. This detector setting guarantees that the collected signal results in an approximately incoherent atomic-number contrast STEM image.

References

1. Tenne, D. A. *et al.* Probing Nanoscale Ferroelectricity by Ultraviolet Raman Spectroscopy. *Science* **313,** 1614-1616 (2006).

2. Bruchhausen, A. *et al.* Ferroelectricity-Induced Coupling between Light and Terahertz-Frequency Acoustic Phonons in $BaTiO_3/SrTiO_3$ Superlattices. *Phys. Rev. Lett.* **101**, 197402 (2008).

3. Soukiassian, A. *et al.* Growth of Nanoscale $BaTiO_3/SrTiO_3$ Superlattices by Molecular-Beam Epitaxy. *J. Mater. Res.* **23,** 1417-1432 (2008).

4. Lanzillotti-Kimura, N. D. *et al.* Enhancement and Inhibition of Coherent Phonon Emission of a Ni Film in a $BaTiO_3/SrTiO_3$ Cavity. *Phys. Rev. Lett.* **104,** 187402 (2010).

5. Hlinka, J. *et al.,* Soft-Mode Spectroscopy of Epitaxial $BaTiO_3/SrTiO_3$ Superlattices. *Phys. Rev. B* **82,** 224102 (2010).

DOI: 10.1038/NMAT3826

6. Kathan-Galipeau, K. *et al.* Quantification of Internal Electric Fields and Local Polarization in Ferroelectric Superlattices. *ACS Nano* **5**, 640-646 (2011).

7. Kathan-Galipeau, K. *et al.* Direct Determination of the Effect of Strain on Domain Morphology in Ferroelectric Superlattices with Scanning Probe Microscopy. *J. Appl. Phys.* **112,** 052011 (2012).

8. Cahill, D. G., Goodson, K., & Majumdar, A., Thermometry and Thermal Transport in Micro/Nanoscale Solid-State Devices and Structures. *J. Heat Transfer* **124**, 223 (2002).

9. Hopkins, P. E. *et. al.* Criteria for Cross-plane Dominated Thermal Transport in Multilayer Thin Film Systems during Modulated Laser Heating. *J. Heat Transfer* **132**, 081302 (2010).

10. Thomsen, J. T. C., Grahn, H. T. & Maris, H. J. *Phys. Rev. B* **34**, 4129 (1986).

11. Thomsen, J. T. C., Strait, J., Vardeny, Z. & Maris, H. J. *Phys. Rev. Lett.* **53**, 989 (1984).

12. Touloukian, Y. S. & Buyco, E. H. *Thermophysical Properties of Matter: Specific Heat: Metallic Elements and Alloys* (John Wiley & Sons Ltd, 1970).

13. Shomate, C. H. *J. Am. Chem. Soc.* **68**, 964–966 (1946).

14. Todd, S. S. & Lorenson, R. E. *J. Am. Chem. Soc.* **74**, 2043–2045 (1952).

15. Koh, Y. & Cahill, D. *Phys. Rev. B* **76**, 075207 (2007).

16. Gundrum, B. Cahill, D. & Averback, R. *Phys. Rev. B* **72**, 1–5 (2005).

17. Cahill, D. G. Analysis of heat flow in layered structures for time-domain thermoreflectance. *Rev. Sci. Instrum.* **75,** 5119 (2004).

18. Schmidt, A. J., Chen, X. & Chen, G. *Rev. Sci. Instrum.* **79**, 114902 (2008).

19. Oh, D.-W. *et al.* Thermal conductivity as a metric for the crystalline quality of $SrTiO_3$ epitaxial layers. *Appl. Phys. Lett.* **98,** 221904 (2011).

20. Simkin, M. & Mahan, G. Minimum thermal conductivity of superlattices. *Phys. Rev. Lett.* **84,** 927 (2000).

21. Costescu, R.,Wall, M., & Cahill, D. *Phys. Rev. B* **67**, 054302 (2003).

22. Cheaito, R. *et al.* Experimental Investigation of Size Effects on the Thermal Conductivity of Silicon-Germanium Alloy Thin Films. *Phys. Rev. Lett.* **109,** 195901 (2012).

23. Chen, G. Size and Interface Effects on Thermal Conductivity of Superlattices and Periodic Thin-Film Structures. *J. Heat Transfer* **119,** 220–229 (1997).

24. Collaboration: Authors and Editors of the LB Volumes III/17A-22A-41A1b: Gallium arsenide (GaAs), phonon dispersion, phonon frequencies and wavenumbers. Madelung, O., Rössler, U., Schulz, M. (ed.). SpringerMaterials - The Landolt-Börnstein Database (http://www.springermaterials.com). DOI: 10.1007/10832182_189.

25. Collaboration: Authors and editors of the volumes III/17H-17I-41E: *$SrTiO_3$ phonon dispersion*. Madelung, O., Rössler, U., Schulz, M. (ed.). SpringerMaterials - The Landolt-Börnstein Database (http://www.springermaterials.com). DOI: 10.1007/10717201_521.

26. Voyles, P. M., Grazul, J. L. & Muller, D. A. *Ultramicroscopy* **96**, 251 (2003).

Figure Captions

Figure S1 RHEED monitoring during growth. a, RHEED oscillations for a $(STO)_2/(CTO)_2$ superlattice grown on an NGO substrate. The oscillations were present throughout the growth of the superlattice film. **b,** RHEED patterns showing the specular and diffracted spots of the substrate before growth and the film after the growth respectively. The strong intensity of the film specular spot suggests that the surface of the sample remains smooth after the growth of the 200-nm film. **c,** RHEED oscillations for a $(STO)_{13}/(BTO)_6$ superlattice grown on an STO

DOI: 10.1038/NMAT3826

substrate. The oscillations were present throughout the growth of the superlattice film. **d,** RHEED patterns showing the specular and diffracted spots of the film at the beginning of growth, and at the end of the growth, respectively. The strong intensity of the film specular spot suggests that the surface of the sample remains smooth after the growth of the 113-nm film.

Figure S2 Schematic of the main components of the TDTR setup used.

Figure S3 Sensitivity of the ratio to Al/CTO-STO Kapitza conductance, *h1*, CTO-STO thermal conductivity, CTO-STO thermal conductivity, κ, and CTO-STO/NGO Kapitza conductance, *h2*. a, at 84 K, **b,** at 142 K and **c,** at 306.7 K.

Figure S4 Sample data and best-fit curves for the $(STO)_1/(CTO)_1$ and $(STO)_3/(CTO)_3$ samples on NGO substrates.

Figure S5 Thermal conductivity values for 200-nm thick STO and CTO films on NGO (110) as a function of temperature.

Figure S6 Thermal conductivity values of 6 different $(STO)_n/(BTO)_m$ superlattices with different period thicknesses as a function of temperature.

Figure S7 Calculated thermal conductivity values using a Simkin-Mahan model. Shown are results for $(STO)_n/(CTO)_m$ superlattices, normalized by division by bulk mean free path, using

literature values of atomic weights and sound velocities for different values of mean free paths of phonons, given in terms of lattice constants (LC).

Figure S8 Calculated thermal conductivity values using interface-dependent mean free path. Shown are results for thermal conductivity of a $(STO)_n/(CTO)_m$ superlattices, with a mean free path obtained using Mathiessen's rule as described in the text. The bulk mean free path is 30 lattice constants and different values of the constant *c* determining effectiveness of interface scattering are shown. The thermal conductivity is normalized to the bulk conductivity.

Figure S9 Reciprocal space maps of superlattices. a, $(STO)_1/(CTO)_1$, **b,** $(STO)_3/(CTO)_3$, **c,** $(STO)_6/(CTO)_6$, and **d,** $(STO)_9/(CTO)_9$ superlattices grown on NGO substrates.

Figure S10 XRD characterization of the $(STO)_m/(BTO)_n$ superlattices. a, Long-range θ-2θ XRD scans of the four high interface density $(STO)_m/(BTO)_n$ samples used for the temperature-dependent TDTR study in Fig. S7. The substrate peaks are indicated by (*). **b,** Long-range θ-2θ XRD scans of the two low interface density $(STO)_m/(BTO)_n$ samples used for the temperature-dependent TDTR study in Fig. S7. **c,** Rocking curve of the **$(STO)_4/(BTO)_3$** superlattice, with a FWHM of 0.0058°.

Figure S11 AFM characterization of an $(STO)_n/(CTO)_m$ superlattice. a, AFM image of size 2.5 μm x 2.5 μm, and **b,** Cross-sectional profile along the line X—X', shown in **a.**

DOI: 10.1038/NMAT3826

Figure S12 Cross-sectional HAADF-STEM characterization of the $(STO)_{30}/(BTO)_1$ superlattice. a, Low-magnification image of the superlattice. **b,** High-resolution image of the superlattice, showing an atomically sharp interface between STO and BTO. Arrows in '**a**' indicate the homoepitaxial interface of the superlattice (STO-first layer) with the STO substrate. Arrows in '**b**' indicate the single unit cell of BTO within the superlattice.

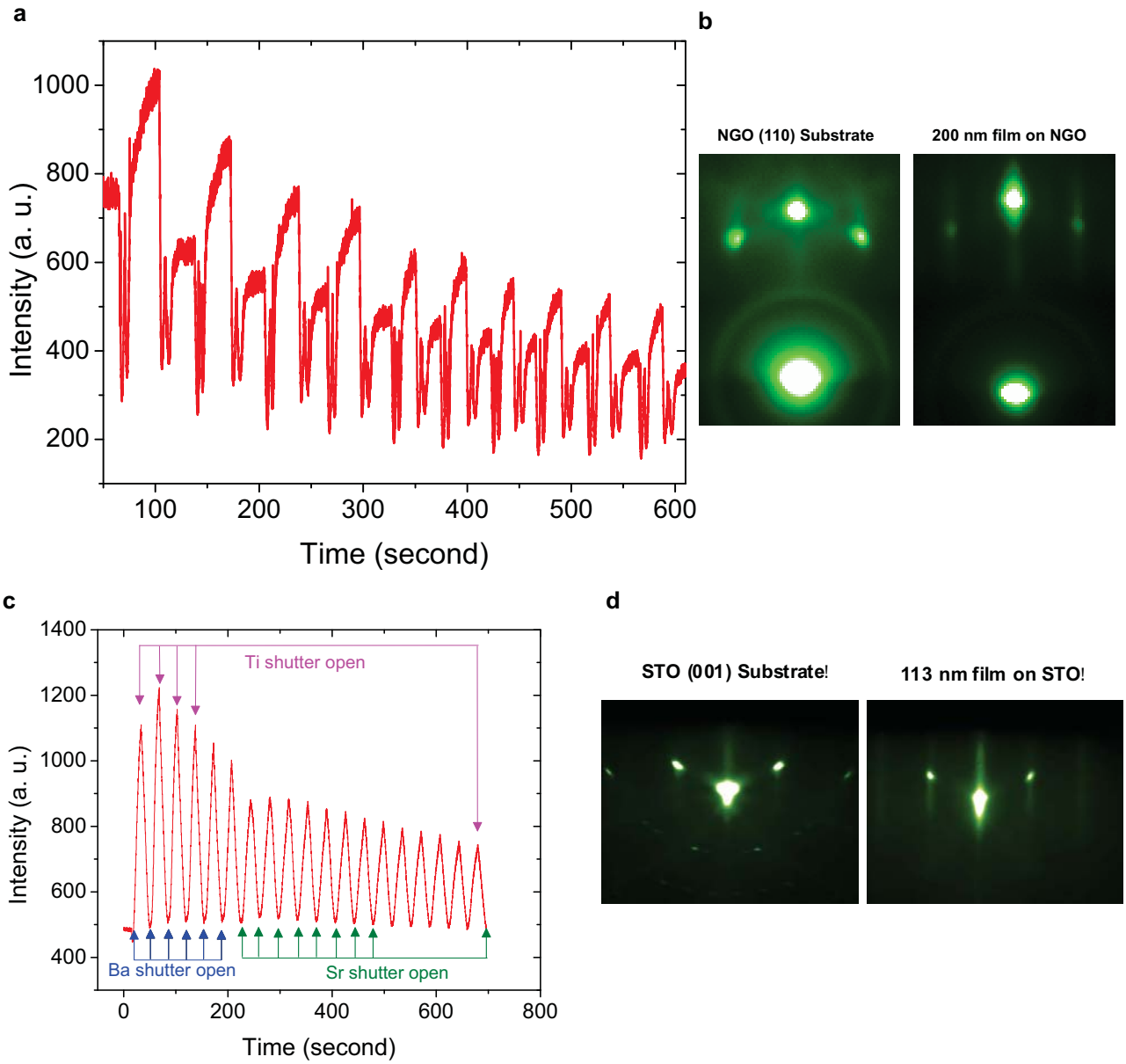

Figure S1 RHEED monitoring during growth. a, RHEED oscillations for a $(STO)_2/(CTO)_2$ superlattice grown on an NGO substrate. The oscillations were present throughout the growth of the superlattice film. **b,** RHEED patterns showing the specular and diffracted spots of the substrate before growth and the film after the growth respectively. The strong intensity of the film specular spot suggests that the surface of the sample remains smooth after the growth of the 200-nm film. **c,** RHEED oscillations for a $(STO)_{13}/(BTO)_6$ superlattice grown on an STO substrate. The oscillations were present throughout the growth of the superlattice film. **d,** RHEED patterns showing the specular and diffracted spots of the film at the beginning of growth, and at the end of the growth, respectively. The strong intensity of the film specular spot suggests that the surface of the sample remains smooth after the growth of the 113-nm film.

DOI: 10.1038/NMAT3826

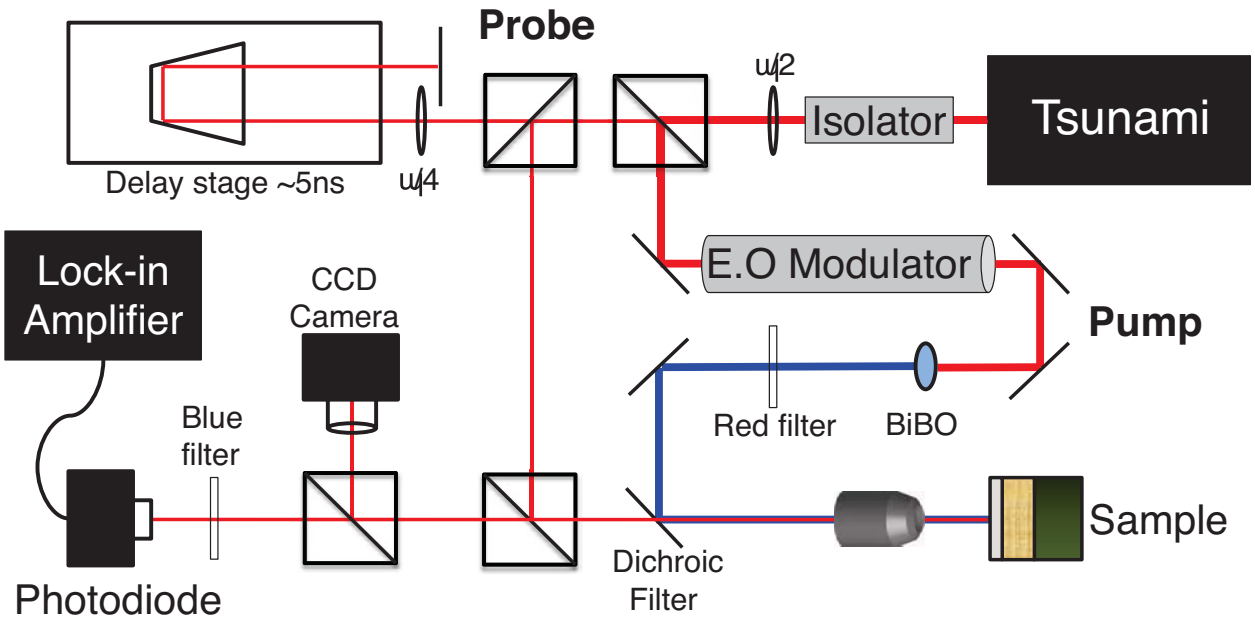

Figure S2 Schematic of the main components of the TDTR setup used.

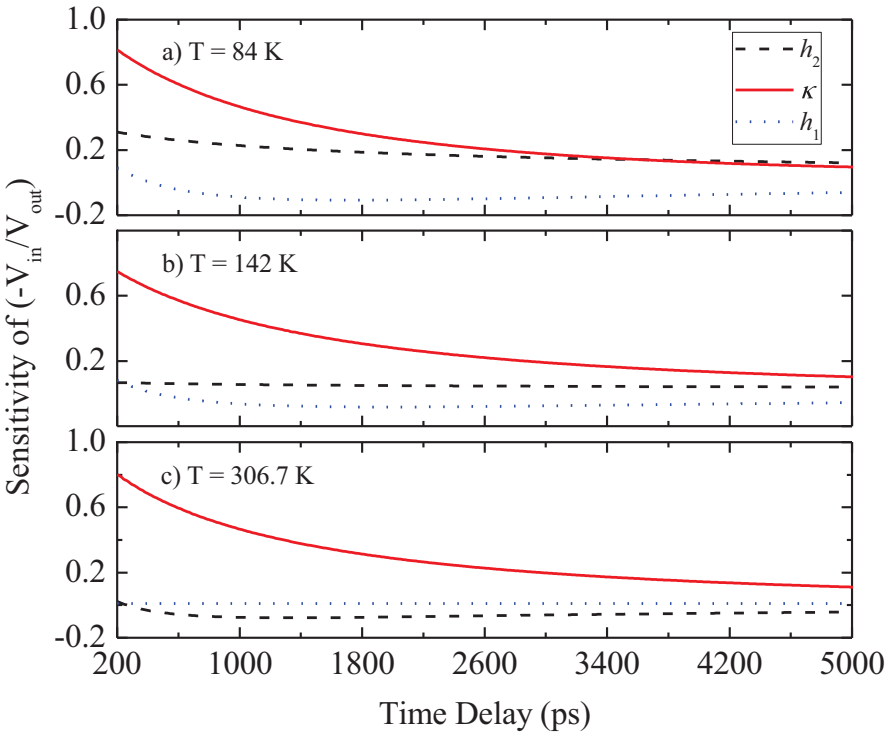

Figure S3 Sensitivity of the ratio to Al/CTO-STO Kapitza conductance, *h1*, CTO-STO thermal conductivity, CTO-STO thermal conductivity, *κ*, and CTO-STO/NGO Kapitza conductance, *h2*. a, at 84 K, **b,** at 142 K and **c,** at 306.7 K.

DOI: 10.1038/NMAT3826

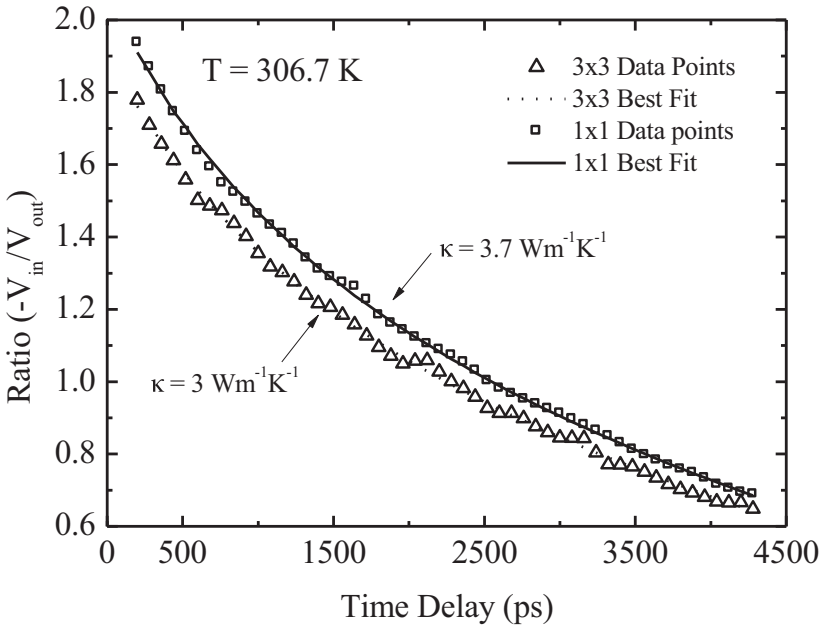

Figure S4 Sample data and best-fit curves for the $(STO)_1/(CTO)_1$ and $(STO)_3/(CTO)_3$ samples on NGO substrates.

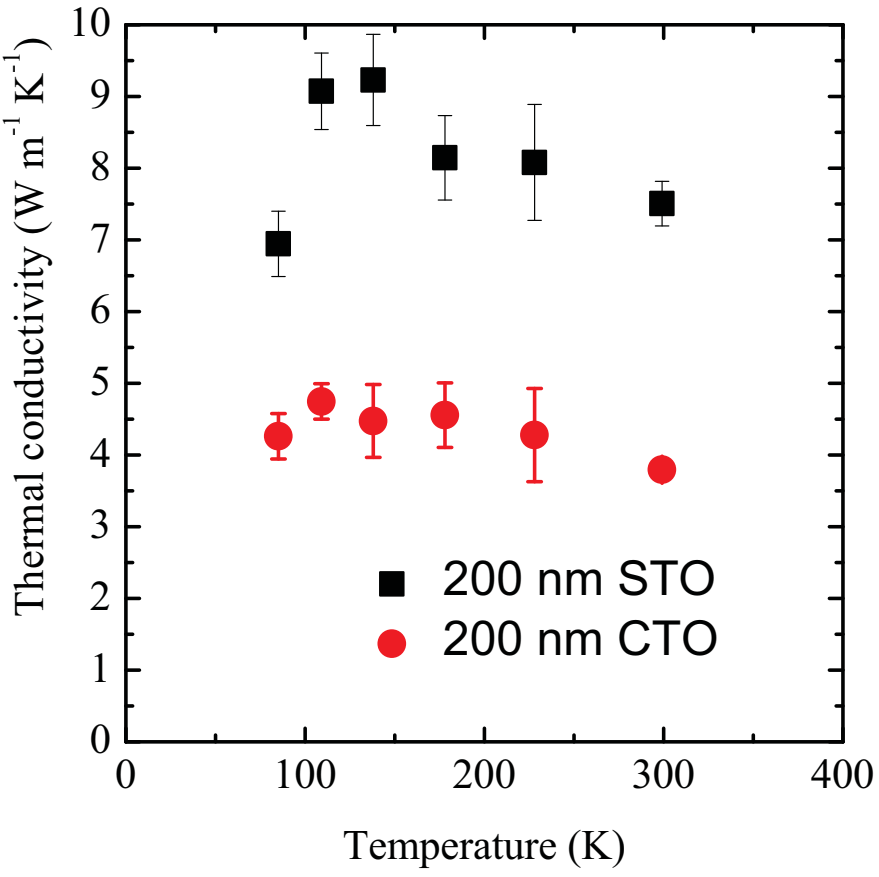

Figure S5 Thermal conductivity values for 200-nm thick STO and CTO films on NGO (110) as a function of temperature.

DOI: 10.1038/NMAT3826

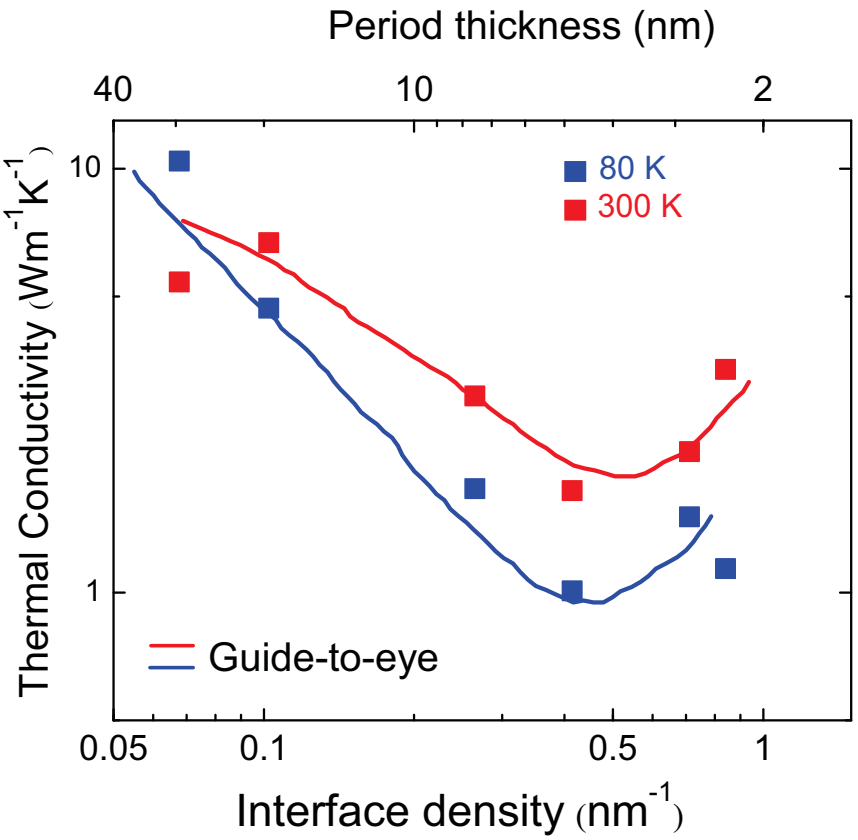

Figure S6 Thermal conductivity values of 6 different $(STO)_n/(BTO)_m$ superlattices with different period thicknesses as a function of temperature.

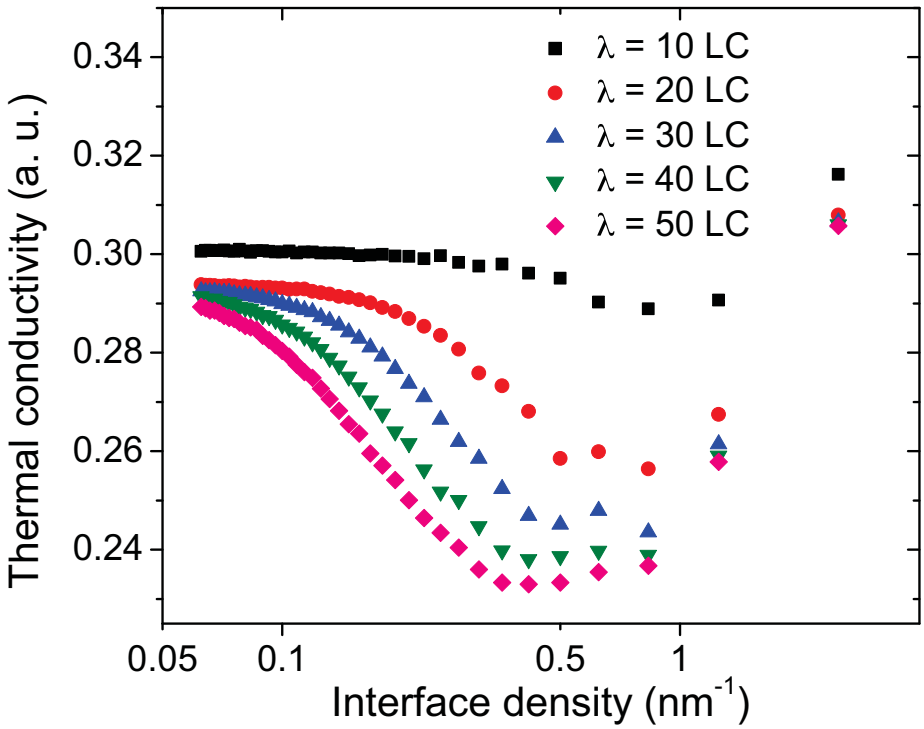

Figure S7 Calculated thermal conductivity values using a Simkin-Mahan model. Shown are results for $(STO)_n/(CTO)_m$ superlattices, normalized by division by bulk mean free path, using literature values of atomic weights and sound velocities for different values of mean free paths of phonons, given in terms of lattice constants (LC).

DOI: 10.1038/NMAT3826

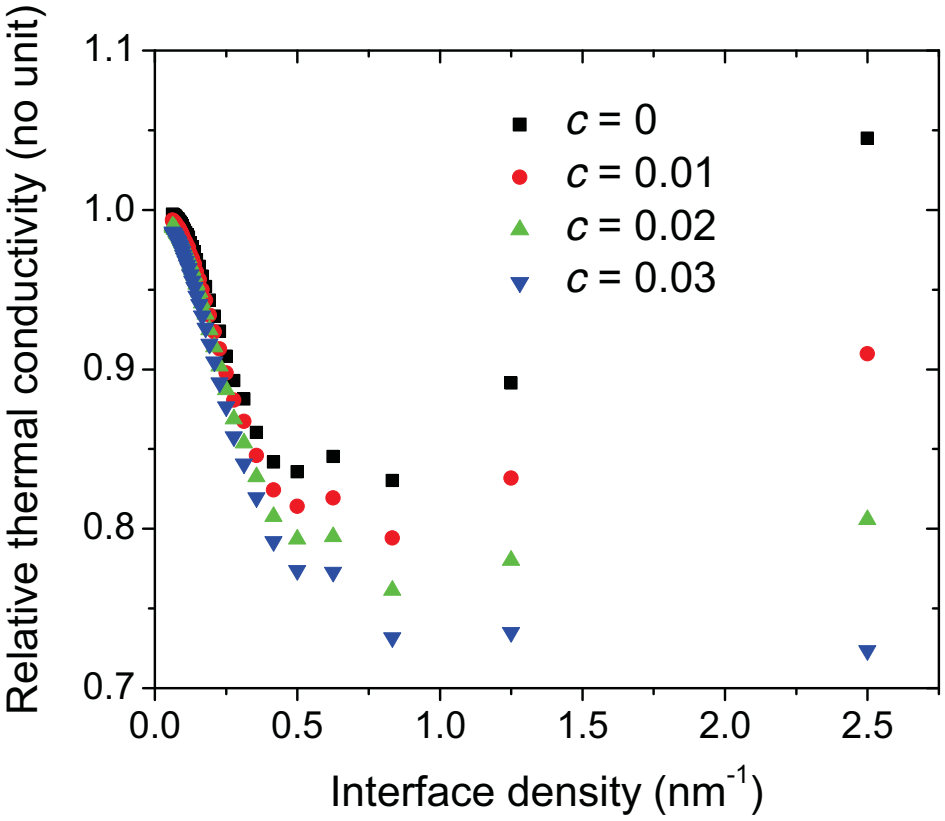

Figure S8 Calculated thermal conductivity values using a interface-dependent mean free path model. Shown are results for thermal conductivity of a $(STO)_n/(CTO)_m$ superlattices, with a mean free path obtained using Mathiessen's rule as described in the text. The bulk mean free path is 30 lattice constants and different values of the constant c determining effectiveness of interface scattering are shown. The thermal conductivity is normalized to the bulk conductivity.

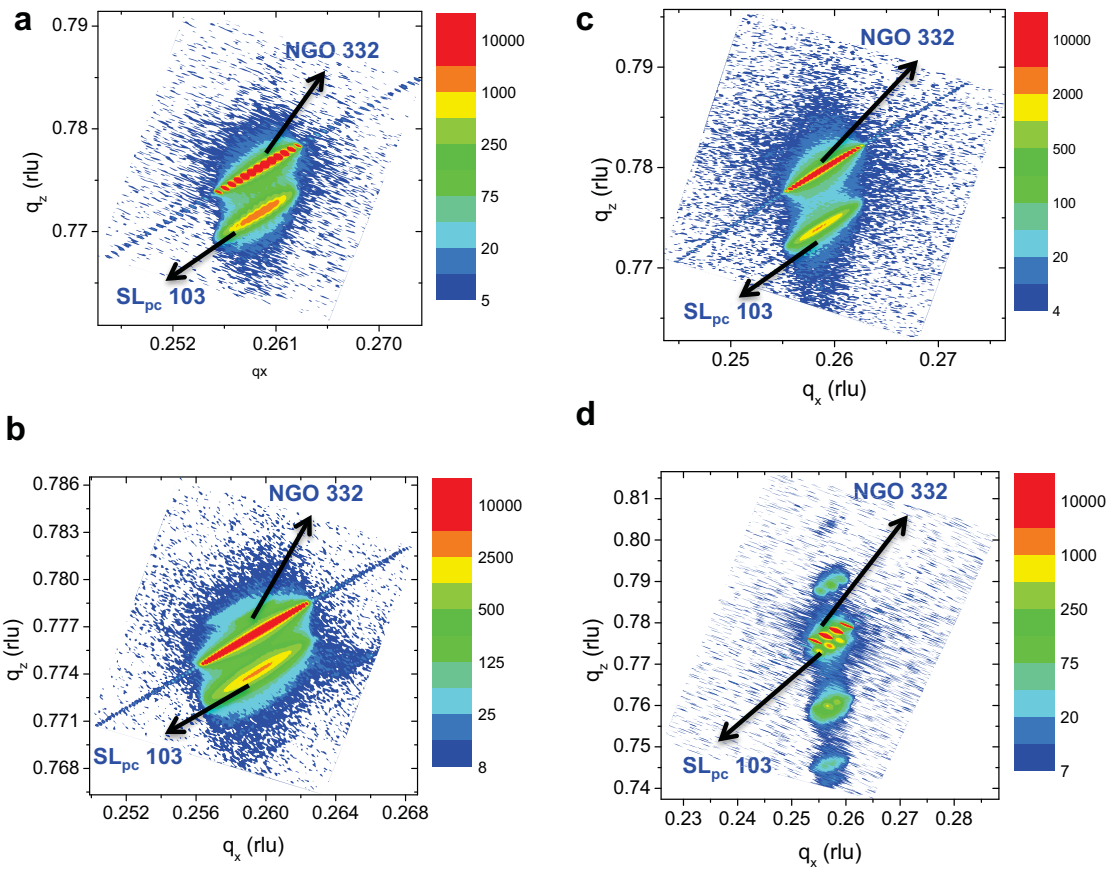

Figure S9 Reciprocal space maps of superlattices. a, $(STO)_1/(CTO)_1$, **b,** $(STO)_3/(CTO)_3$, **c,** $(STO)_6/(CTO)_6$, and **d,** $(STO)_9/(CTO)_9$ superlattices grown on NGO substrates.

DOI: 10.1038/NMAT3826

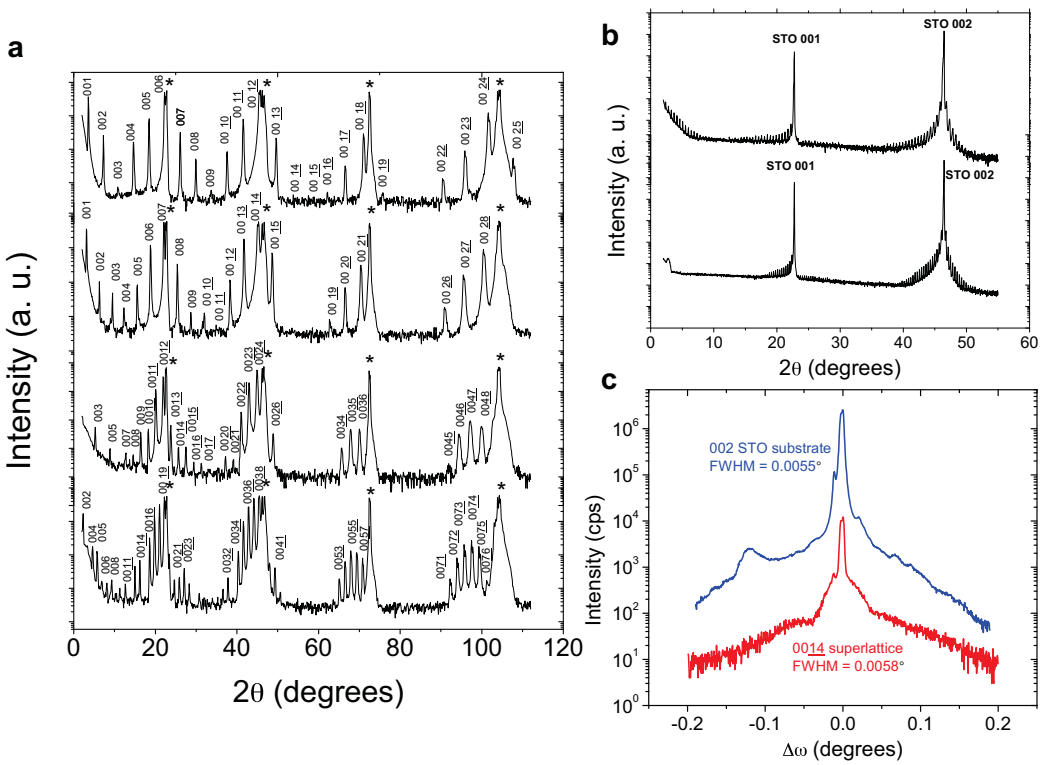

Figure S10 XRD characterization of the $(STO)_m/(BTO)_n$ superlattices. a, Long-range θ-2θ XRD scans of the four high interface density $(STO)_m/(BTO)_n$ samples used for the temperature-dependent TDTR study in Fig. S7. The substrate peaks are indicated by (*). **b,** Long-range θ-2θ XRD scans of the two low interface density $(STO)_m/(BTO)_n$ samples used for the temperature-dependent TDTR study in Fig. S7. **c,** Rocking curve of the **$(STO)_4/(BTO)_3$** superlattice, with a FWHM of 0.0058°.

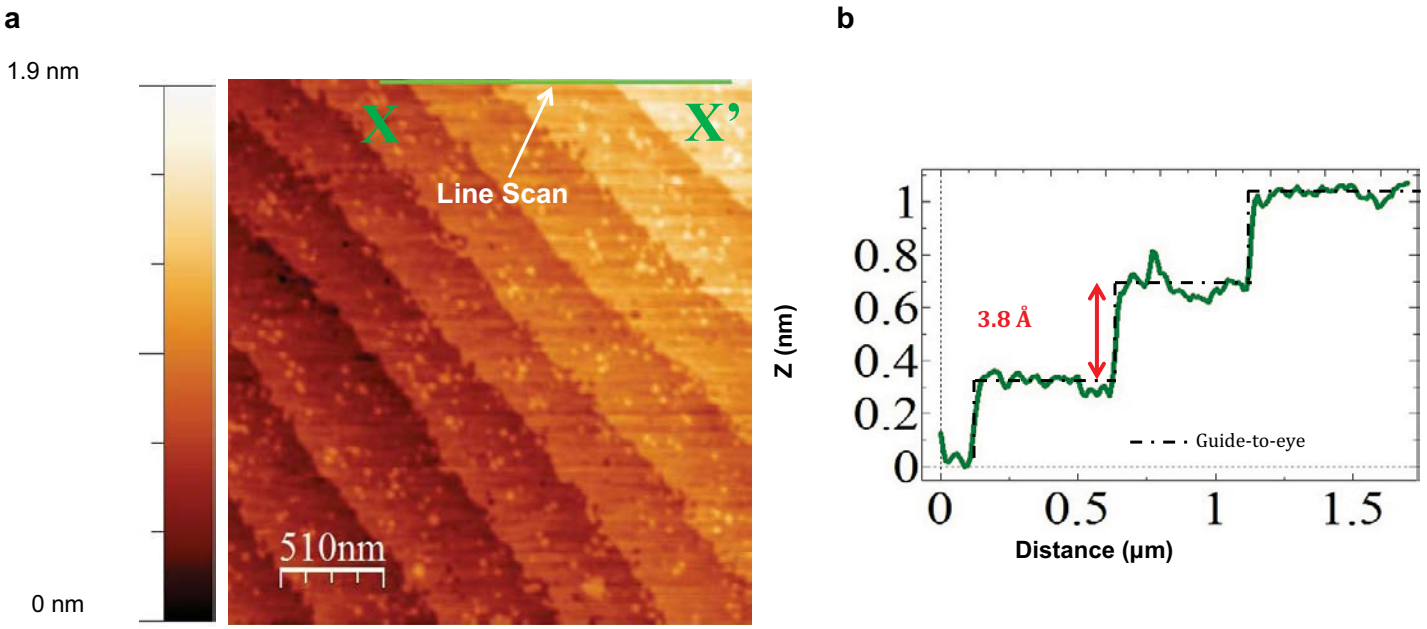

Figure S11 AFM characterization of an $(STO)_n/(CTO)_m$ superlattice. **a,** AFM image of size 2.5 μm x 2.5 μm, and **b,** Cross-sectional profile along the line X—X', shown in **a.**

DOI: 10.1038/NMAT3826

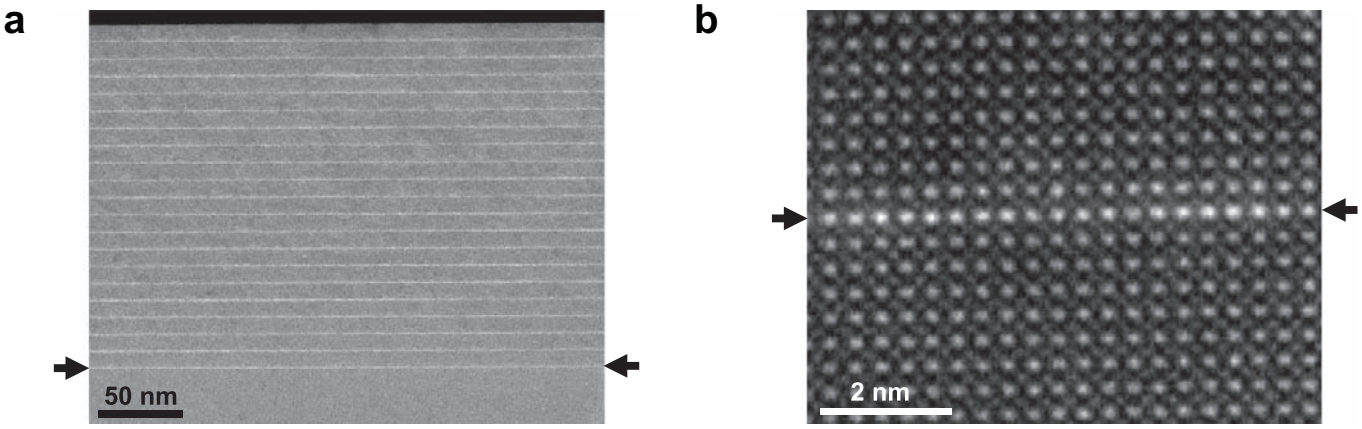

Figure S12 Cross-sectional HAADF-STEM characterization of the $(STO)_{30}/(BTO)_1$ superlattice. a, Low-magnification image of the superlattice. **b,** High-resolution image of the superlattice, showing an atomically sharp interface between STO and BTO. Arrows in '**a**' indicate the homoepitaxial interface of the superlattice (STO-first layer) with the STO substrate. Arrows in '**b**' indicate the single unit cell of BTO within the superlattice.